MJFAS
Malaysian Journal of Fundamental and Applied Sciences

Abdul Malek *et al.* | Malaysian Journal of Fundamental and Applied Sciences, Vol. 20 (2024) 1288-1307

RESEARCH ARTICLE

Improving Classification Performance of Spatial Filters in Mammographic Microcalcifications Images Using Persistent Homology

Aminah Abdul Malek[a,b*], Mohd Almie Alias[a], Fatimah Abdul Razak[a], Mohd Salmi Md Norani[a]

[a]Department of Mathematical Sciences, Faculty of Science & Technology, Universiti Kebangsaan Malaysia, UKM, Bangi 43600, Selangor, Malaysia; [b]Mathematical Sciences Studies, College of Computing, Informatics, and Mathematics, Universiti Teknologi MARA (UiTM) Negeri Sembilan Branch, Seremban Campus, 70300 Seremban, Negeri Sembilan, Malaysia

Abstract Noise and artefacts in mammogram images can obscure important indicators of microcalcifications, complicating accurate diagnosis. While traditional spatial filters can reduce noise and are effective to some extent, they often fail to enhance features crucial for classification. This study uses persistent homology (PH) to evaluate and improve the classification performance of various spatial filters on mammogram images. The evaluation process involves converting filtered images into persistence diagrams (PDs) to capture topological features. These diagrams are then vectorised into PH features for classification using a neural network classifier. This study also examines further filtering of PDs from filtered images to enhance classification performance. Using the Digital Database for Screening Mammography (DDSM) and Mammographic Image Analysis Society (MIAS) datasets, we evaluate Median, Wiener, Gaussian, and Bilateral filters alone and integrate them with PH-based filtering. Results show significant classification improvements, with Wiener filters achieving 96.33% accuracy on the DDSM dataset (up from 57.38%) and Gaussian filters reaching 85.33% on the MIAS dataset (up from 73.33%). These findings demonstrate the potential of PH-based filters to enhance diagnostic accuracy in breast cancer detection by refining topological features and effectively reducing noise.

Keywords: Spatial filter, breast cancer, classification, mammogram, persistent homology.

***For correspondence:**
p112233@siswa.ukm.edu.my

Received: 17 July 2024
Accepted: 16 Oct 2024

Introduction

Breast cancer remains a major health concern for women globally. In 2020, more than 2.3 million women were diagnosed with breast cancer, resulting in 685,000 deaths [1]. The incidence of breast cancer is projected to exceed over 3 million new cases annually by the year 2040, with 1 million anticipated fatalities [2]. Preventive measures, including imaging screening, play a crucial role in early detection, significantly improving patient survival rates [3]. Among the various screening techniques, mammography has been proven to identify early-stage cancers[4].

Microcalcifications (MCCs) are suspicious signs that often require further investigation, appearing in about one-third of malignant lesions detected during mammography [5], [6]. Benign MCCs are typically larger, rounder in shape, fewer, and more uniform. In contrast, clusters of small-sized and irregular-shaped MCCs may indicate early signs of cancer (malignant cases) [7]. Accurate classification of MCCs as benign or malignant is essential for early diagnosis and effective treatment planning. However, the noise and artefacts in mammogram images affecting the identification of MCCs pose a significant challenge [8].

Advancements in image processing have improved the accuracy of microcalcification detection [9], [10]. Enhancing any process could improve the entire system's performance [11]. Pre-processing, particularly image denoising, is crucial [12]. Traditional spatial filters like Median, Weiner, Gaussian, and Bilateral filters are commonly used for noise reduction in mammograms [13], [14], [15]. Every method has its own set of benefits and drawbacks. The Median Filter handles outliers without amplifying noise, yet it may also blur image details and thin lines, even at low noise densities [15], [16]. The Wiener filter is helpful in adapting to varying noise levels but tends to blur sharp edges and incompletely filter the noise [17]. The Gaussian filter smooths images effectively, but it can also obscure high-frequency details [18]. The Bilateral filter preserves edges while reducing noise and can effectively maintain the structural details of an image [19]. Nevertheless, it may struggle with high noise levels and is computationally intensive, making it less practical for large datasets [20]. Although traditional filters have effectively reduced common types of noise in mammographic images, such as Gaussian noise, salt and pepper noise, and speckle noise, most studies evaluate these filters using image quality metrics such as Peak Signal Noise Ratio (PSNR) and Structural Similarity Index (SSIM) [21], [22]. However, there is a lack of studies examining how these filters influence the classification performance of mammographic images, particularly for detecting microcalcifications. This study addresses this gap by investigating how traditional filters, both individually and combined with a persistent homology approach, affect the classification performance of a neural network.

Persistent Homology (PH) is a core tool in topological data analysis (TDA), known for extracting multi-scale topological features from data [23], [24]. PH has been applied across various domains, especially in medical image processing, where PH has been leveraged for tasks such as tumour segmentation in colorectal cancer [25] and biomedical image segmentation [26]. Furthermore, PH features such as connected components, loops, and voids, which are captured across different scales and represented in persistence diagrams, have been effectively utilised in classification tasks, including identifying hepatocellular ballooning in liver biopsies [27], diagnosing prostate cancer [28], classifying breast tumours [29], hepatic tumour classification [30], and analysing eye fundus images [31].

Despite these advancements, the application of PH in image denoising, particularly in mammographic analysis, remains underexplored. Our previous work [32] introduced PH-based filtering approach for noise reduction in mammogram images. Unlike traditional spatial filters, this method operates on persistent diagrams (PDs) derived from PH, aiming to preserve the intrinsic features of microcalcifications and thereby enhance the discriminatory information for classification tasks.

Persistence Diagrams (PDs), a key topological descriptor from PH, capture the birth and death of features like connected components and loops as pixel intensity varies. PDs effectively summarise these features' significance by plotting their lifespan on a half-plane above the diagonal [33]. Points far from the diagonal indicate prominent features, while those close to the diagonal are interpreted as noise [29]. The distinct ability of PH to differentiate between significant and noise features drives our investigation, utilising PH to evaluate filtering techniques and exploring its potential to improve classification performance.

In PH, the topological features from PDs can be converted into a format compatible with machine-learning models. Two common methods for this conversion are Persistent Entropy (PE) and Persistent Image (PI). PE measures the complexity of topological features by assessing the distribution of the lifespans, providing a robust metric for datasets with varying topological structures [34]. For instance, Leykam *et al*. [35] used PE to detect dark solitons, demonstrating its effectiveness in analysing complex topological structures. Similarly, Rammal *et al*. [36] utilised PE as input in a machine-learning model to diagnose prostate cancer, while Yen and Cheong [34] applied it to the stock market analysis in Singapore and Taiwan. On the other hand, Persistent Image (PI) transforms points in PDs into fixed-size images [37], leveraging image-based capabilities for effective data analysis. The effectiveness of PI in medical imaging is evidenced by Teramoto *et al*. [38] in classifying hepatocellular ballooning in liver biopsies, Asaad *et al*. [39] in breast tumour classification using mammogram scans, and Oyama *et al*. [37] in hepatic tumour classification using MRI images.

This study expands on our previous work by leveraging PH to evaluate the impact of spatial filters on the classification performance of a neural network using PH features. The primary goals are: i) to assess how different spatial filters affect the classification of microcalcifications and ii) to integrate PH-based filtering with spatial filters to enhance classification performance. This research aims to contribute to more accurate and reliable breast cancer detection and diagnosis by addressing the challenges of noise and artefact removal in mammogram images.

Methodology

This study uses the PH approach to evaluate how various spatial filters applied to mammogram images affect the classification performance of a neural network. The evaluation process involves several key steps: transforming all filtered images into PD to capture their topological features, vectorising these PD using PH features; and classifying the vectorised features with a Neural Network Classifier. We propose further filtering the PDs to enhance classification accuracy. The proposed framework is illustrated in Figure 1, encompasses the entire process from image acquisition to classification, integrating spatial filtering and PH analysis to improve microcalcifications' classification for early breast cancer diagnosis. The main stages of this framework are described below.

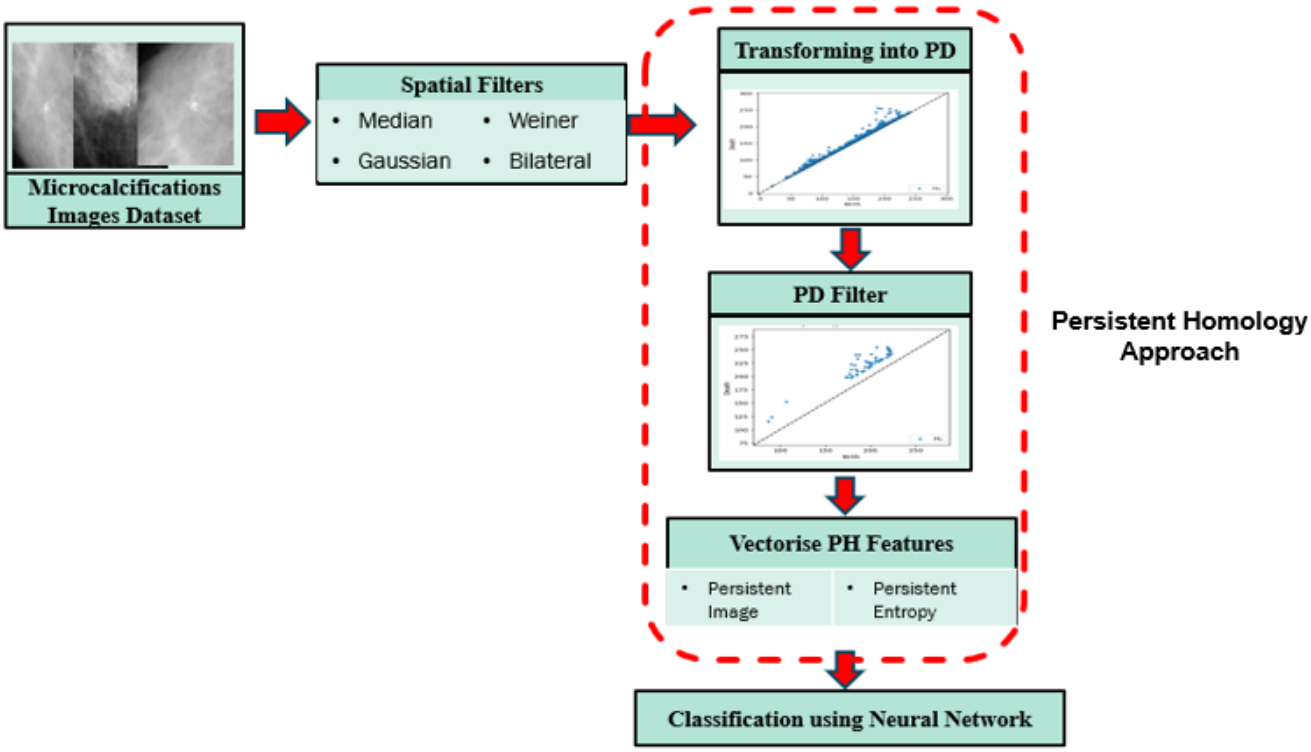

Figure 1. Illustration of proposed framework

Dataset

Two publicly available datasets containing regions of interest (ROI) with microcalcifications were used. The first dataset is from the MIAS dataset, containing 26 image patches mammography films with the abnormality's location given by the specialists [40]. The patches include three types of background tissue: fatty, fatty glandular, and dense glandular. The ROI size of each image is 200 x 200 pixels. The second dataset is from the digital screening mammography (DDSM) database, consisting of 244 image patches randomly selected with the size of 300 x 300 pixels [41]. The image labels for both datasets are described in Table 1. Although both datasets contain many mammograms, not all of them exhibit microcalcifications. Therefore, the number of microcalcification patches is significantly lower than the total number of images in the datasets.

Table 1. Image labels for mammographic microcalcifications in both datasets

	Benign	Malignant	**Total**
MIAS	13	13	**26**
DDSM	122	122	**244**

Spatial Filters

Spatial filtering techniques are widely employed to address noise-related problems and enhance an image's quality [42]. These techniques adjust pixel values based on their neighbouring pixels. This study compares the following spatial filtering methods:

Median Filter

The median filter is a non-linear spatial filtering technique commonly used in the pre-processing of mammography images [43]. It replaces each pixel value with the median of the surrounding pixels within a sliding window over the image [44]. Mathematically, for a pixel , the median filtered value is

$$M(x,y) = median\{I(x+i, y+j)\} \quad (1)$$

where (i, j) are the coordinates of the pixels within the window centred at (x, y). The window size is a critical factor in the operation of the median filter. It determines the range of neighbouring pixels that are taken into account. Larger windows offer more effective noise reduction but can also blur image details. On the other hand, smaller windows preserve details better but may not be as effective at reducing noise [45].

Gaussian Filter

The Gaussian filter is a technique that smooths and reduces noise by convolving the image with a Gaussian kernel. It assigns higher weights to central pixels and lower weights to those further away [46]. The filtered image $G'(x, y)$ is obtained using [47]

$$G'(x,y) = \sum_{i=-k}^{k} \sum_{j=-k}^{k} I(x+i, y+j) * G(i,j) \quad (2)$$

where $G(i,j) = e^{-\frac{i^2+j^2}{2\sigma^2}}$, σ is the standard deviation of the Gaussian distribution and k determines the kernel size, with the summation covering all pixels in the window centred at (x, y). An important parameter of the Gaussian function is σ (sigma), which controls the level of smoothness where a larger sigma value results in more significant smoothing.

Wiener Filter

The Wiener filter is used to reduce noise in images while preserving important details by minimising the mean square error between the estimated and the original image. In the spatial domain, the filter operates over a local neighbourhood or kernel, which determines how much of the surrounding pixel information is used to compute the output for each pixel. The mathematical formulation of the Wiener filter in the spatial domain is [48]

$$\hat{f}(x,y) = \frac{H^*(u,v)}{H^2(u,v) + \left(\frac{P_n(u,v)}{P_S(u,v)}\right)} G(u,v) \quad (3)$$

where $f(x,y)$ is the original image, $H^*(u,v)$ is the complex conjugate of the Fourier transform of the degradation filter, $H^2(u,v)$ is the momentum square of the degradation filter, $G(u,v)$ is the degraded image in the frequency domain, $P_n(u,v)$ and $P_s(u,v)$ are the power spectra of the noise and the signal, respectively. The output image $\hat{f}(x,y)$ is obtained by multiplying the observed image by the Wiener filter in the frequency domain, followed by an inverse Fourier transform to return to the spatial domain. An essential parameter of the Wiener filter is the kernel size, which affects the filter's performance and the balance between noise reduction and detail preservation.

Bilateral Filter

The Bilateral Filter stands out for its ability to smooth images while preserving edge details [49]. It replaces each pixel's intensity value by averaging only those pixels with similar intensities within a specified neighbourhood [50]. This Bilateral filter ensures that edges, typically identified by sudden intensity changes, remain unaltered during the smoothing process. The formulation is as follows:

$$I_f(p) = \frac{1}{W_p} \sum_{q \in S_D} I(q) \times \exp\left(-\frac{\|p-q\|^2}{2\sigma_r^2}\right) \times \exp\left(-\frac{|I(p)-I(q)|^2}{2\sigma_s^2}\right) \quad (4)$$

where $I_f(p)$ is the filtered intensity value at pixel *p*, $I(q)$ is the intensity value at pixel *q* within the neighbourhood *S* with diameter *D*, W_p is the normalisation factor, σ_r is sigma space which controls the spatial proximity influences the filtering process and σ_s is sigma color space determines the influence of colour intensity among neighbouring pixels.

Table 2 presents the parameter configurations for the spatial filters employed in this study. These parameters reflect the best-performing configurations within our experimental framework, determined using cross-validation to achieve the highest accuracy for each filter applied to the MIAS and DDSM datasets.

Table 2. Parameter settings for spatial filters

	Median	Gaussian	Wiener	Bilateral
MIAS	WS = [3,3]	Sigma = 1.0	KS= [3,3]	D=10, S=15, s=15
DDSM	WS = [3,3]	Sigma = 0.5	KS = [3,3]	D=15, S=20, s=30

Based on Table 2, the term 'WS' in the Median filter refers to the 'Window Size' used to determine the area around each pixel contributing to the median calculation. This area is typically a square grid of pixels, like a 3x3 matrix. Gaussian filters use the 'Sigma' value to represent the standard deviation of the blur effect. Higher values of 'Sigma' indicate more blur in the image [21]. On the other hand, 'KS' or 'Kernel Size' in Wiener filters defines the dimensions of the sliding window that moves across the image to apply the filtering process. The Bilateral filter uses 'D' to refer to the diameter of the pixel neighbourhood considered for filtering, 'S' and 's' to denote the 'Sigma Color Space' and 'Sigma Space', respectively.

Persistent Homology

Persistent homology (PH) provides a profound understanding of the image's structure corresponding to the *k*-th homology group (H_k), such as connected components (H_0), loops (H_1), voids (H_2), and higher dimensional features. The first step in computing persistent homology is constructing complexes from the image. The cubical complexes are ideal for representing a two-dimensional grayscale image, which are intricate geometric shapes consisting of a finite union of *n*-cubes, such as vertices (0-cubes), edges (1-cubes), and squares (2-cubes) [51]. In this image, each pixel is considered as a 2-cube square. These squares are grouped to form a cubical complex, as shown in Figure 2.

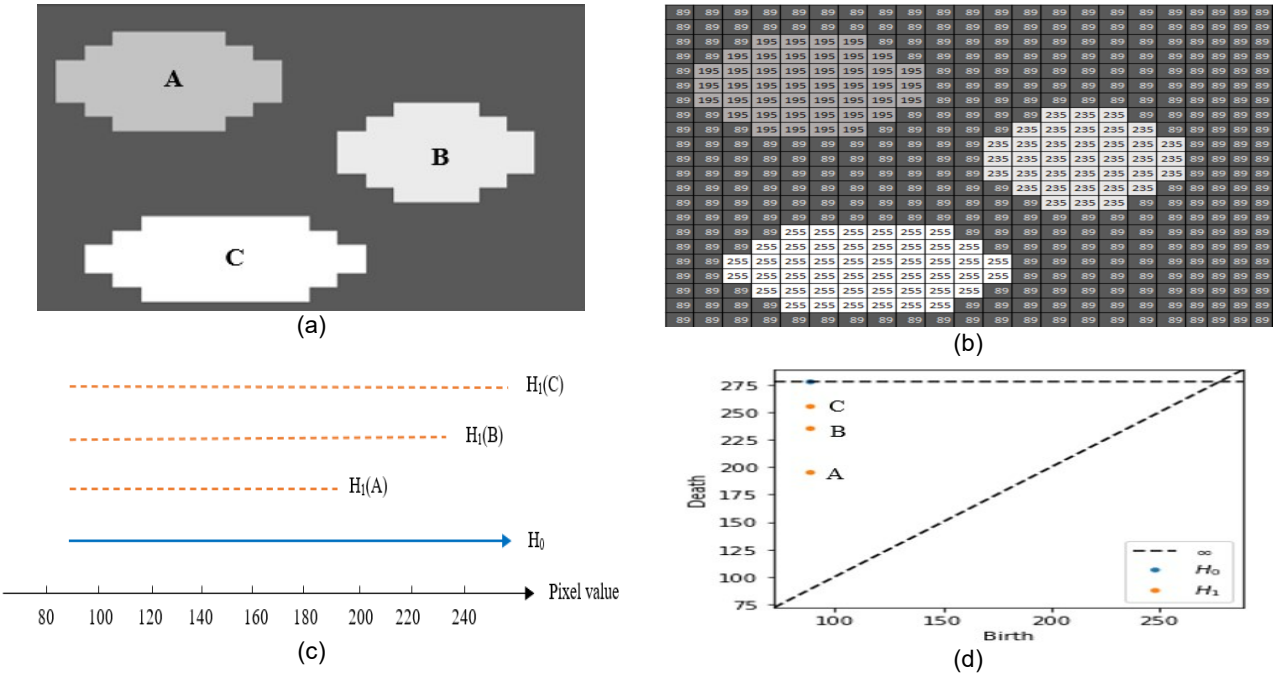

Figure 2. Illustration of cubical complex formation in grayscale images using persistent homology tools. (a) sample test image, (b) pixel values of the image, (c) the barcode of topological features and (d) the persistent diagram

The grayscale test image in Figure 2(a) contains three objects, A, B, and C, placed against a uniform background. These objects are differentiated by their pixel values, as Figure 2(b) illustrates. Object A has a value of 195, B is 235, and C is at the maximum of 255, against the background value of 89. These pixels constitute a cubical complex, which is then analysed topologically. The barcode diagram in Figure 2(c) illustrates topological features' birth and death points, with the blue line showing the connected component of the image, indicating areas of contiguous pixel values. As the filtration value increases, this line demonstrates the development and eventual merging of distinct regions within the image. Meanwhile, the objects in the image are captured by the three loops in orange dashed lines, which track the existence of these features through their creation and filling (in homological terms, their birth and death in H_1). Moreover, the persistent diagram (PD) in Figure 2(d) is yet another representation of the barcode by plotting these features on a plane, with the x-axis indicating the birth points and the y-axis indicating the death points, providing a clear visualisation of their persistence within the cubical complex framework.

The differences between death and birth points on the diagram represent the feature's lifespan, providing a measure of feature persistency [52]. Points far from the diagonal (long lifespan) indicate their significance or robustness features in the data, whereas points that lie close to the diagonal (short lifespan) are often considered potential noise [35]. The persistent diagram in Figure 2(d) concretely quantifies these features, with the lifespan of each feature being critically assessed by the distance between its birth and death points. Such distinction is pivotal for our study's focus on 1-dimensional holes (H_1) due to their relevance in identifying microcalcifications shown as white spots in mammographic images.

Transitioning from the conceptual to the practical, Figure 3 illustrates examples of PDs for both benign and malignant microcalcifications in the DDSM dataset. The PDs demonstrate that images with similar structures exhibit similar patterns [53]. Specifically, the benign PDs (Figure 3a) show topological features associated with long-lived lifespans, while malignant PDs (Figure 3b) have shorter lifespans, resembling noise. This differentiation highlights the significance of PH in discerning meaningful patterns from noise, establishing it as a crucial marker in our analysis.

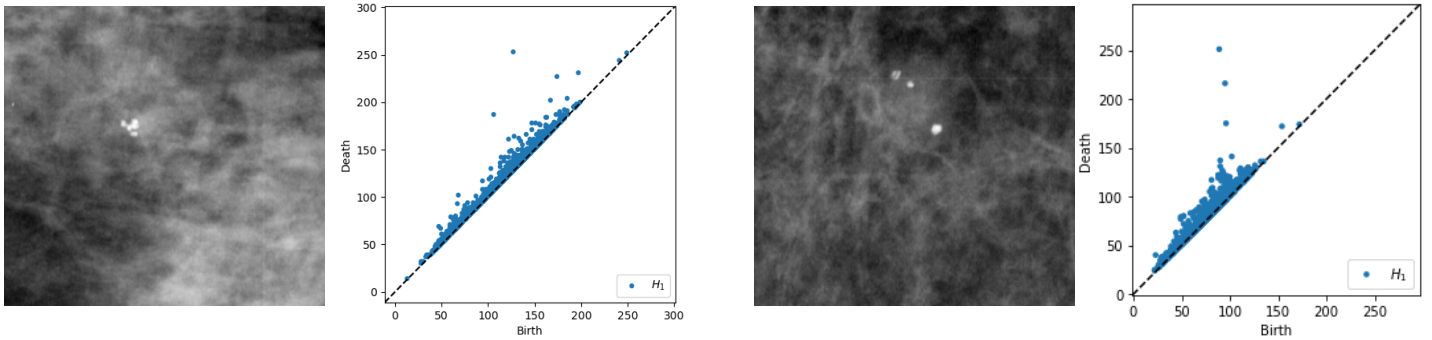

a) Benign microcalcifications

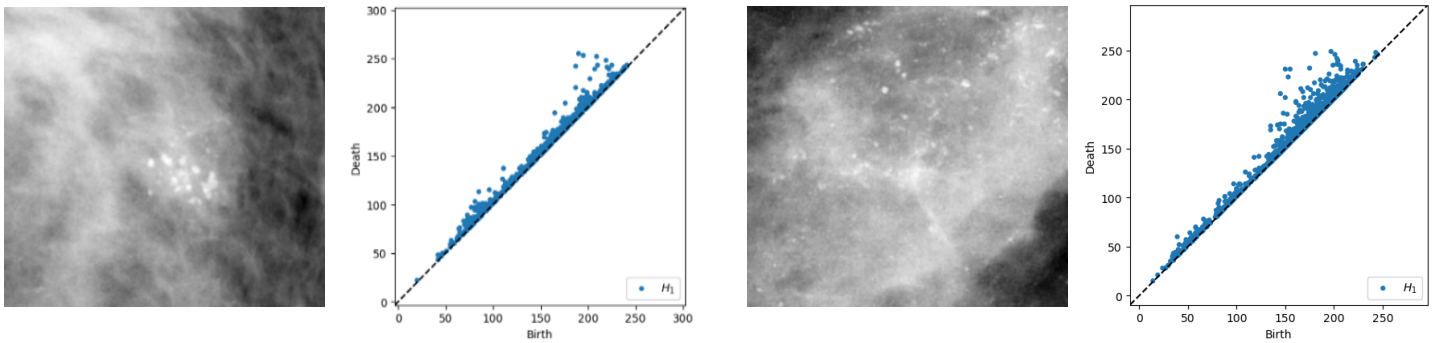

b) Malignant microcalcifications

Figure 3. The H_1 PDs of benign and malignant microcalcifications in the DDSM dataset

PH-Based Filtering

The PH-based filtering approach provides an innovative method for image denoising by operating on PDs rather than directly on the image. In our previous study, we proposed a multi-level filtering technique using PDs, to effectively filter and classify mammographic microcalcification images, as detailed in [32]. This method demonstrated significant potential in enhancing the classification accuracy of machine learning techniques.

In this study, we expand our previous work by integrating spatial filters with the PH-based filter to enhance the classification performance further. The proposed approach applies spatial filters to preprocess the images and then derives PDs from the filtered images. The PDs are subsequently filtered based on the maximum lifespan of topological features. The filtering process consists of the following steps:

Step 1: For each filtered image, obtain the PD for 1-dimensional loops (H_1):

$$PD_{H_1} = \{(b_i, d_i) \mid i = 1,2,3,...,n\} \tag{5}$$

where b_i and d_i represent the birth and death values for topological feature *i*.

Step 2: Calculate the lifespan of each point in the PD. The lifespan is calculated as the difference between the death and birth values:

$$lifespan(i) = d_i - b_i \tag{6}$$

Step 3: Find the maximum lifespan.

$$\max(lifespan) = \max\{lifespan(i) = 1,2,3,...,n\} \tag{7}$$

Step 4: Perform incremental noise filtering on PD. Filtering (*P*) is performed based on a certain percentage of the maximum lifespan. Points that have a lifespan exceeding a certain threshold value are retained.

$$P_{k\%} = \{i \mid lifespan(i) > k \times \max(lifespan)\} \tag{8}$$

where *k* represents the filtering percentage.

Step 5: Obtain the corresponding points in the PD. For each filtering level, we need to obtain the points in the persistent diagram whose lifespan matches the filtered range:

$$PD_{k\%} = \{(b_i, d_i) \mid (b_i, d_i) \in PD_{H_1} \wedge i \in P_{k\%}\} \tag{9}$$

The complete algorithm for PH-based filtering is summarised in Algorithm 1.

Algorithm 1 PH-based Filtering using PD
Input: *n* ← number of images in a dataset
  for *i* =1,2, 3, …., *n* **do**
    I ← load the *i*th image from the dataset.
    ***PD*H1** ← Obtain the persistent diagram of H_1 (loops)
    lifespan ← Calculate the lifespan (death – birth)
    max_lifespan ← Obtain the max(***lifespan***)

    for each ***point*** in ***PD*1 do**
    for *threshold* = 'δ' to 1 where '$0 < \delta < 1$' **do**
      if ***point***(***lifespan***) > ***threshold * max_lifespan***
        Add ***point*** to ***filter_[threshold *100]%***
Output: ***filter_[threshold *100]%*(*points*)**

Based on this algorithm, the threshold value corresponds to the percentage of denoising. We used a 20% filter for the MIAS dataset and 30% for the DDSM dataset for comparison purposes, as proposed by [32].

PH Features

After filtering, the H_1 data is transformed into a vector using PH features to form a feature set for the machine learning model to assess the classification performance. Persistent entropy and persistent image are used for vectorisation, providing topological features.

A) Persistent Entropy (PE)

PE measures the disorder in the distribution of lifespan (persistence). Let PD's lifespan, $\mathrm{l} = |death - birth|$ points. The entropy of PD is defined as [51]

$$\varepsilon(PD) = \sum_{j=1}^{n} \frac{\mathrm{l}_j}{S(\mathrm{l}_j)} \log\left(\frac{\mathrm{l}_j}{S(\mathrm{l}_j)}\right) \tag{10}$$

where j is the index of lifespans, n is the total number of lifespans (or features) and $S(\mathrm{l}_j)$ is the sum of the lifespan in the PD. Every PD will produce one entropy value. A zero PE value indicates the presence of a single or dominant feature, while *N* number of features consists of PE of $\log(N)$. In scenarios where noise-induced features exhibit similar persistence levels, higher entropy values occur [35].

B) Persistent Image (PI)

PI is a technique proposed by Adams *et al*. [54] to convert PDs into fixed-dimension vectors that are suitable for machine learning. To construct PI, a PD's persistence points (birth and death coordinates) are rotated $45°$. The rotated PD denoted as *R* is then discretised into the persistent surface (ρ) in (x, y) coordinated defined as

$$\rho R(x,y) = \sum_{(b,d) \in R} g_{(b,d)}(x,y).\, f(b,d) \tag{11}$$

where $g(b,d)$ is a Gaussian smoothing function defined as

$$g_{(b,d)}(x,y) = \frac{1}{2\pi\sigma^2} e^{-[(x-b)^2+(y-d)^2]/2\sigma^2} \tag{12}$$

and $f(b,d) \geq 0$ are non-negative weighting functions. The PI is derived by integrating the persistence surface function $\rho R(x,y)$ over each pixel. Our experiments use a pixel size of 1, yielding one vectorised PI value per PD. The weighting function, $f(b,d)$ is based on the persistence values [54], and the Gaussian function's smoothing parameter, σ is set to 1 by default.

Classification Using Neural Network

A neural network (NN) is a network system that is widely used in machine learning. The basic building block of a NN is the neuron, which can have adjustable weights to facilitate learning. The complexity of the network depends on the number of layers [55]. The primary network structure consists of three layers that group the neurons. These layers consist of input, hidden, and output layers. The NN architecture of this study is shown in Figure 4. The network utilises features derived from PH, which are PI and PE, as input layers. These features are unique in their ability to capture nuanced topological structures and the complexities inherent in data. A bias term ensures that the network maintains flexibility and adaptability. As the data travels through the network, it passes through a hidden layer of neurons. Throughout the network, the sigmoid activation function introduces non-linearity, enabling the model to capture intricate patterns. The processed data then moves to the output layer, with two neurons representing benign and malignant classifications. This network's design emphasises the potential of combining traditional neural network structures with persistent homology features.

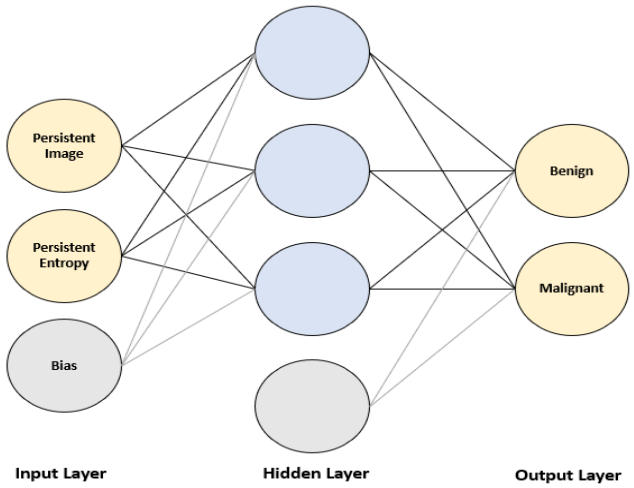

Figure 4. The Neural Network Architecture

Performance Evaluation

The effectiveness of each filtering technique is measured based on the classification performance metrics. A fundamental tool in classification evaluation is the confusion matrix, which presents a tabular number of predicted classes against the actual classes [56]. This matrix consists of four elements described in Figure 5.

		Predicted Class	
		Benign	**Malignant**
True Class	**Benign**	True Positives (TP)	False Negatives (FN)
	Malignant	False Positives (FP)	True Negatives (TN)

Figure 5. The confusion matrix

The confusion matrix provides insights into how well the classification model's predictions match the actual outcomes. This matrix is used to calculate other performance metrics such as accuracy, precision, recall, f-measure, and specificity, which are defined as follows [57].

- *Accuracy (Acc).* The percentage of images correctly classified to the total number of images. It gives an overall measure of how often the classifier is correct.

$$Acc = \frac{TP + TN}{TP + TN + FP + FN} \times 100\% \tag{13}$$

- *Precision* (Pr). The percentage of correctly predicted benign images to the total images predicted as benign. It describes the accuracy of the positive predictions, where high precision implies that the false positive rate is low.

$$\Pr = \frac{TP}{TP + FP} \times 100\% \tag{14}$$

- *Recall (Rc).* It is also called sensitivity. It measures the percentage of correctly predicted benign images to the total actual benign images. It tells us about the classifier's ability to detect positive cases. High recall means that the classifier correctly identified most of the positive cases.

$$Rc = \frac{TP}{TP + FN} \times 100\% \tag{15}$$

- *F-measure (Fm).* It provides a single score that balances the trade-off between precision and recall. The score can be used to determine the correctness of the test dataset.
-

$$Fm = \left(2 \times \frac{\mathrm{Pr} \times Rc}{\mathrm{Pr} + Rc} \right) \times 100\% \tag{16}$$

- *Specificity (Sp).* The percentage of correctly predicted malignant images compared to the actual malignant images. High specificity means that the classifier correctly identified most of the malignant cases.

$$Sp = \frac{TN}{TN + FP} \times 100\% \tag{17}$$

In addition, the overall effectiveness of filtering techniques can also be measured using the area under the curve (AUC) obtained by the receiver operating characteristic curve (ROC). The ROC curve plots the true positive rate (TPR), called recall, versus the false positive rate (FPR). The FPR mismeasures the number of benign cases identified as malignant compared to the total number of benign instances. This analysis will provide valuable insights into how each filtering method impacts the performance of various classifiers in distinguishing benign from malignant microcalcifications.

Implementation Details

In this study, the spatial filters were implemented in Python using well-established libraries for image processing, such as the Bilateral filter using the OpenCV library, while the Gaussian and Median filters employed the 'ndimage' module from the SciPy library, which offers a comprehensive collection of multidimensional image processing routines. Additionally, the 'signal' module in SciPy facilitates the Wiener filter application, which is equipped to perform advanced signal processing operations.

For the PH computation, the cubical complex filtration and PD are generated using Cubical Ripser Software [58], while the vectorised topological features consisting of PI and PE features can be obtained using the Scikit-TDA library written in Python. Finally, the Rapid Miner Studio is used for the classification model with a fivefold cross-validation. Each experimental test uses 11th Gen Intel(R) Core(TM) i7-11800H, CPU 2.30 GHz, 16 GB memory, and NVIDIA Geforce RTX 3050Ti for the graphics card.

Results and Discussion

In this study, we employed the PH approach to evaluate how various spatial filtering techniques, including Median, Gaussian, Wiener, and Bilateral filters, affect the classification performance of a neural network. The evaluation includes transforming filtered images into Persistence Diagrams (PD), vectorising these PD using PH features, and classifying the vectorised features with a Neural Network Classifier. The impact of further filtering the PD on classification performance is explored. As an illustration, we show samples of malignant images from the DDSM dataset to demonstrate the filtered image produced through spatial filtering techniques alongside the corresponding PD in Figure 6. The Median filter effectively reduces noise while preserving edges, enhancing the visibility of microcalcifications. The Gaussian filter smoothens images, reducing noise and blurring some fine details. The Wiener filter balances reducing noise and preserving features, keeping important structures while moderately reducing noise. The Bilateral filter demonstrates significant noise reduction, as shown by the decrease in the number of dots in the PDs, indicating fewer irrelevant topological features. Despite blurring fine details, it still preserves significant topological features.

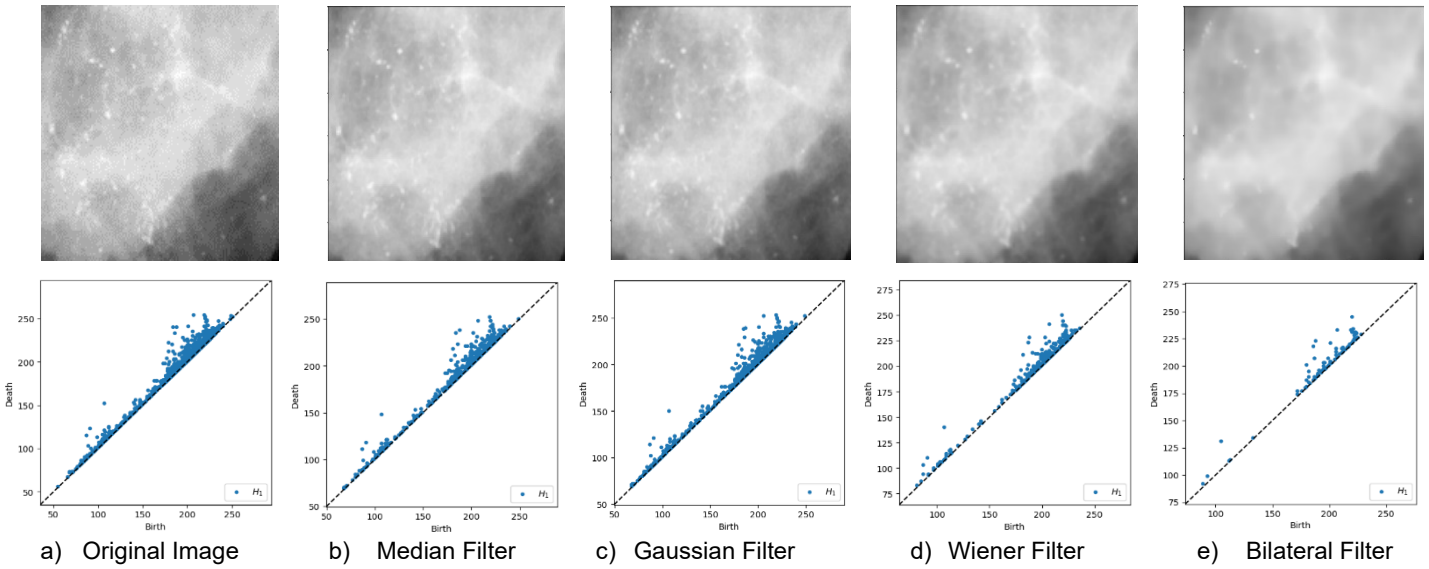

a) Original Image b) Median Filter c) Gaussian Filter d) Wiener Filter e) Bilateral Filter

Figure 6. Comparison of spatial filters applied to the malignant image and the corresponding PD

In Figure 6, the points along the diagonal of the PDs generally represent noise, as these features have short lifespans and are less likely to correspond to meaningful structures like microcalcifications. In contrast, the points further from the diagonal represent more significant topological features, such as microcalcifications, which persist across multiple filtration scales. While spatial filters effectively reduce some types of noise, they may also unintentionally blur or diminish microcalcifications, particularly if the filtering parameters (e.g., kernel size, sigma values) are not carefully tuned.

To address this limitation, we propose the implementation of PH-based filtering. This method involves filtering the PDs to remove diagonal noise features prior to vectorising the topological features. Figure 7 provides an example of integrating PH-based filtering with spatial filters, demonstrating the improvements over the PDs shown in Figure 6. This combination allows for a more robust extraction of meaningful topological features while eliminating noise-related artefacts that spatial filters alone cannot fully address.

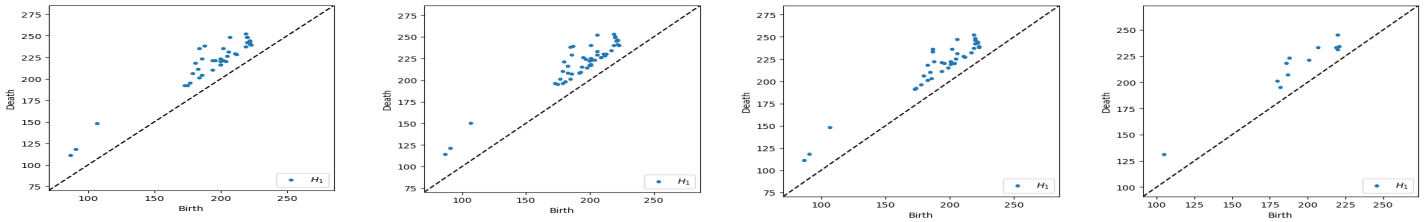

a) Median Filter b) Gaussian Filter c) Wiener Filter d) Bilateral Filter

Figure 7. Example of integrated PH-based filtering with spatial filters

By eliminating these noise elements, the quality of the topological information used for classification is significantly enhanced, leading to more accurate and robust detection of microcalcifications. This additional PH-based filtering step refines the extracted features, ensuring that only the most prominent topological structures are retained for the classification process. In the following section, we will first present the feature extraction results, followed by the classification performance of the neural networks for each filtering technique in DDSM and MIAS datasets.

The Vectorise PH Features

The results of vectorising PH features for the original images, spatial filters and integrated PH-based filters in DDSM and MIAS datasets are shown in Figures 8 and 9, respectively. Each scatter plot point represents the value of PE versus PI for 244 images in DDSM and 26 images in MIAS datasets. Figures

8(a) and 9(a) show the scatter plots of the original images without any spatial filtering applied. As seen in these plots, there is significant overlap between the benign and malignant classes, indicating that it is challenging to distinguish between two classes based solely on topological features without filtering. When examining the spatial filter features only, as in Figures 8 and 9 (b), there is still considerable overlap between the benign and malignant classes, particularly in the core regions of the scatter plots. This highlights the challenges in distinguishing between classes. The Bilateral filter shows a tighter clustering of benign and malignant cases, suggesting it performs well in reducing noise while preserving important features. However, combining spatial filters with PH-based filtering, as shown in Figures 8 and 9 (c), results in significantly improved separation of benign and malignant classes. This is demonstrated by the reduced overlap and more distinct clustering in the scatter plots, particularly for the Gaussian and Wiener filters in the DDSM dataset and the Gaussian filter in the MIAS dataset. These results suggest that PH-based filtering effectively removes diagonal noise features and enhances the distinctiveness of topological features. In the next section, we present the classification performance, demonstrating how the refined topological features improve classification accuracy in distinguishing between benign and malignant cases.

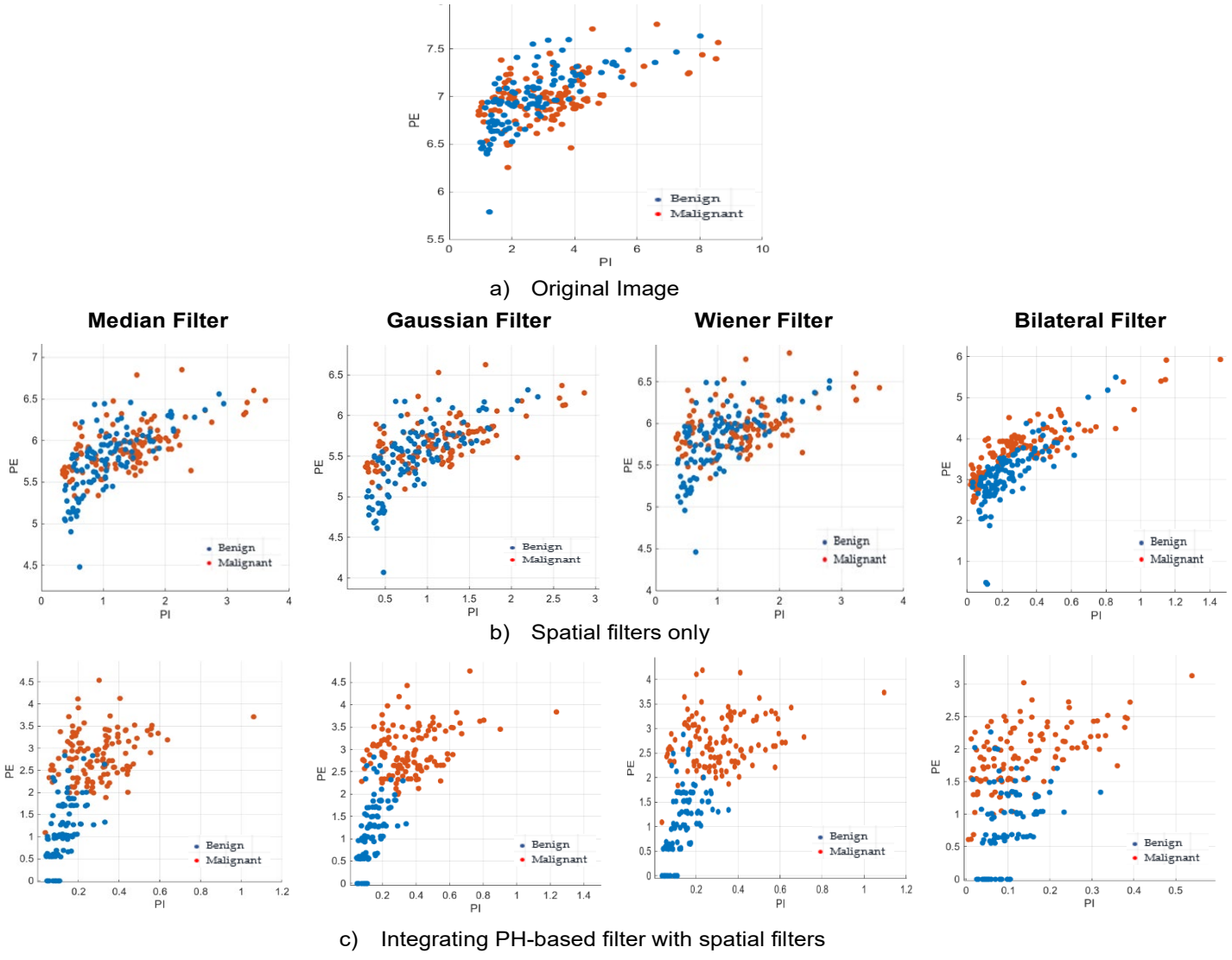

Figure 8. Scatter plot comparison of PH features for spatial filters and integrated PH-based filtering in the DDSM dataset

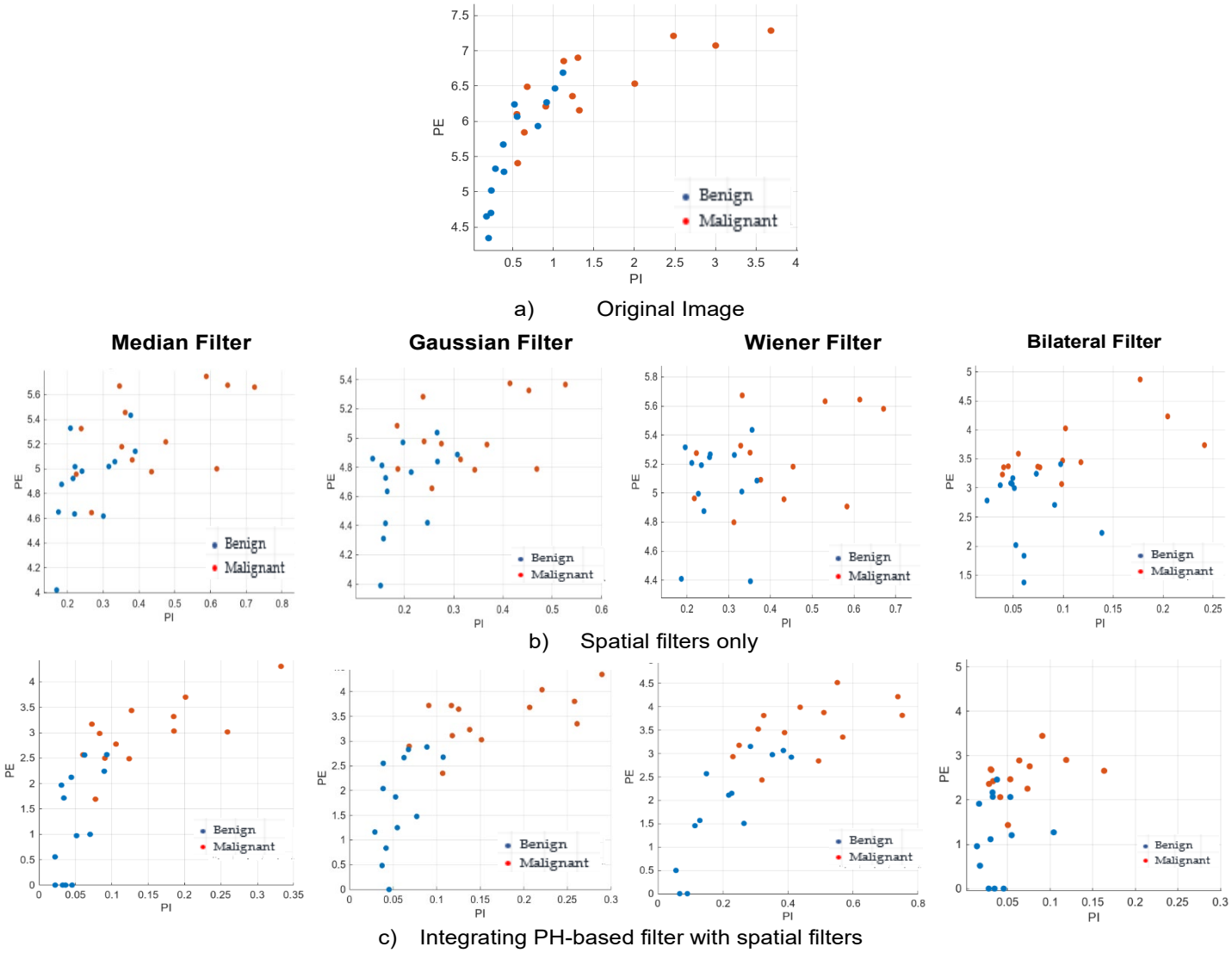

Figure 9. Scatter plot comparison of PH features for spatial filters and integrated PH-based filtering in the MIAS dataset

The Classification Performance

The confusion matrices depicted in Figures 10 and 11 serve as the basis for evaluating the effectiveness of the filters in distinguishing between benign and malignant cases. Figures 10 and 11 (a) show the performance of the original images without any spatial filtering. As expected, without filtering, there is a considerable number of misclassifications in both benign (B) and malignant (M) cases, indicating that without any form of enhancement, it is challenging to distinguish between the two classes accurately. Figures 10 and 11(b) depict the performance of spatial filters alone in both datasets. The Median filter demonstrates a balanced performance but with a notable number of misclassifications in both benign and malignant cases. The Bilateral filter achieves the best performance among the spatial filters alone, displaying fewer misclassifications.

When integrated with pH-based filtering, all the spatial filters show significant improvement, as shown in Figures 10 and 11(c). It reduces the number of misclassifications across both datasets, with the Gaussian and Wiener filters demonstrating the most noticeable improvements. This suggests that PH-based filtering enhances the ability of spatial filters to preserve critical topological features while reducing noise, leading to better classification performance.

True Class \ Predicted Class	B	M
B	83	39
M	53	69

a) Original image

Median Filter

True Class \ Predicted Class	B	M
B	75	47
M	46	76

Gaussian Filter

True Class \ Predicted Class	B	M
B	82	40
M	53	69

Wiener Filter

True Class \ Predicted Class	B	M
B	62	60
M	33	89

Bilateral Filter

True Class \ Predicted Class	B	M
B	90	32
M	37	85

b) Spatial filters only

True Class \ Predicted Class	B	M
B	110	12
M	3	119

True Class \ Predicted Class	B	M
B	114	8
M	4	118

True Class \ Predicted Class	B	M
B	115	7
M	2	120

True Class \ Predicted Class	B	M
B	106	16
M	14	108

c) Integrating PH-based filter with spatial filters

Figure 10. Confusion matrices for spatial filters and Integrated PH-based filtering in the DDSM dataset

True Class \ Predicted Class	B	M
B	9	4
M	4	9

a) Original image

Median Filter

True Class \ Predicted Class	B	M
B	11	2
M	4	9

Gaussian Filter

True Class \ Predicted Class	B	M
B	9	4
M	3	10

Wiener Filter

True Class \ Predicted Class	B	M
B	10	3
M	5	8

Bilateral Filter

True Class \ Predicted Class	B	M
B	10	3
M	3	10

b) Spatial filters only

True Class \ Predicted Class	B	M
B	10	3
M	2	11

True Class \ Predicted Class	B	M
B	11	2
M	2	11

True Class \ Predicted Class	B	M
B	9	4
M	3	10

True Class \ Predicted Class	B	M
B	10	3
M	2	11

c) Integrating PH-based filter with spatial filters

Figure 11. Confusion matrices for spatial filters and Integrated PH-based filtering in the MIAS dataset

The following results detail the classification performances of various spatial filters, both standalone and integrated with PH-based filters, in processing mammographic microcalcification images from both datasets. The tables and figures comprehensively compare accuracy, precision, recall, F-measure, specificity, and AUC for these filters, revealing significant improvements when PH is integrated. For the DDSM dataset, as shown in Table 3, the no-filter configuration, which uses the original images without spatial filters, achieved an accuracy of 62.28%, a precision of 63.65%, a recall of 56.37%, an F-measure of 59.28%, specificity of 67.93%, and an AUC of 0.614. Among the standalone spatial filters, the Bilateral Filter outperforms others with an accuracy of 71.76%, precision of 73.27%, recall of 69.6%, F-measure of 71.19, specificity of 73.87%, and AUC of 0.804. In contrast, the Median, Wiener, and Gaussian filters exhibit lower performance metrics, with accuracies ranging from 56.16% to 60.26% and AUC values from 0.62 to 0.646. These results highlight the limitations of traditional spatial filtering techniques in isolating and classifying microcalcifications effectively. The integration of PH-based filtering shows a marked improvement across all performance metrics, as presented in Table 4. Specifically, the PH-integrated Wiener filter achieves the highest accuracy of 96.33% and an AUC of 0.963, indicating superior discriminatory capability. Similarly, the Gaussian filter shows a notable improvement with an accuracy of 95.1% and an AUC of 0.951. The Median filter also benefits, achieving an accuracy of 93.87% and an AUC of 0.939, while the Bilateral filter, despite its initial strong performance, shows less pronounced improvements post-integration.

Table 3. Classification performances of spatial filters only in the DDSM dataset

Filters	Accuracy	Precision	Recall	F-measure	Specificity	AUC
No Filter	62.28	63.65	56.37	59.28	67.93	0.614
Median Filter	56.16	56.99	58.97	56.85	53.3	0.646
Wiener Filter	57.38	57.98	64.67	60.04	50.03	0.644
Gaussian Filter	60.26	64.97	49.17	54.4	71.33	0.62
Bilateral Filter	71.76	73.27	69.6	71.19	73.87	0.804

Table 4. Classification performances of Integrated PH-based filter with spatial filters in the DDSM dataset

Filters	Accuracy	Precision	Recall	F-measure	Specificity	AUC
Median Filter	93.87	91.28	97.53	94.15	90.23	0.939
Wiener Filter	96.33	94.55	98.33	96.39	94.3	0.96
Gaussian Filter	95.1	93.72	96.7	95.16	93.5	0.951
Bilateral Filter	87.7	87.22	88.47	87.74	86.93	0.877

Shifting to the MIAS dataset, the standalone spatial filters (Median, Bilateral and Gaussian) demonstrate moderate performances, with all three showing improvements over the original image (no-filter), as shown in Table 5. In contrast. the Wiener filter performs the least effectively, with an accuracy of 68.67% and an AUC of 0.684, showing a decline compared to the original image. The integration of PH with spatial filters significantly improves classification performance across all metrics, as shown in Table 6. The Gaussian filter integrated with PH achieved the highest accuracy of 85.33% and an AUC of 0.867. These results indicate that PH can enhance the ability of spatial filters to classify microcalcifications, even in a smaller sample size dataset like MIAS.

Table 5. Classification performances of spatial filters only in the MIAS dataset

Filters	Accuracy	Precision	Recall	F-measure	Specificity	AUC
No Filter	69.33	65	66.67	69.23	70	0.683
Median Filter	76.67	75	83.33	76.48	70	0.767
Wiener Filter	68.67	72	76.67	70.33	60	0.684
Gaussian Filter	73.33	66.67	66.67	72	76.67	0.717
Bilateral Filter	76.67	76.67	76.67	75.14	76.67	0.767

Table 6. Classification performances of Integrated PH-based filter with spatial filters only in the MIAS dataset

Filters	Accuracy	Precision	Recall	F-measure	Specificity	AUC
Median Filter	82	83.3	80	80	86.67	0.833
Wiener Filter	74.67	80	73.33	76	76.67	0.75
Gaussian Filter	85.33	86.67	86.67	85.33	86.67	0.867
Bilateral Filter	82	85	80	81.14	83.33	0.817

Figures 12 and 13 provide a comparative analysis of the classification performance metrics for spatial filters alone (blue bars) and integrated PH-based filtering with spatial filters (orange bars), with the red dashed line representing the performance of the original image without any filtering. This allows us to compare how much spatial filters improve upon the original image's classification performance, and how integrating PH-based filtering further enhances these metrics.

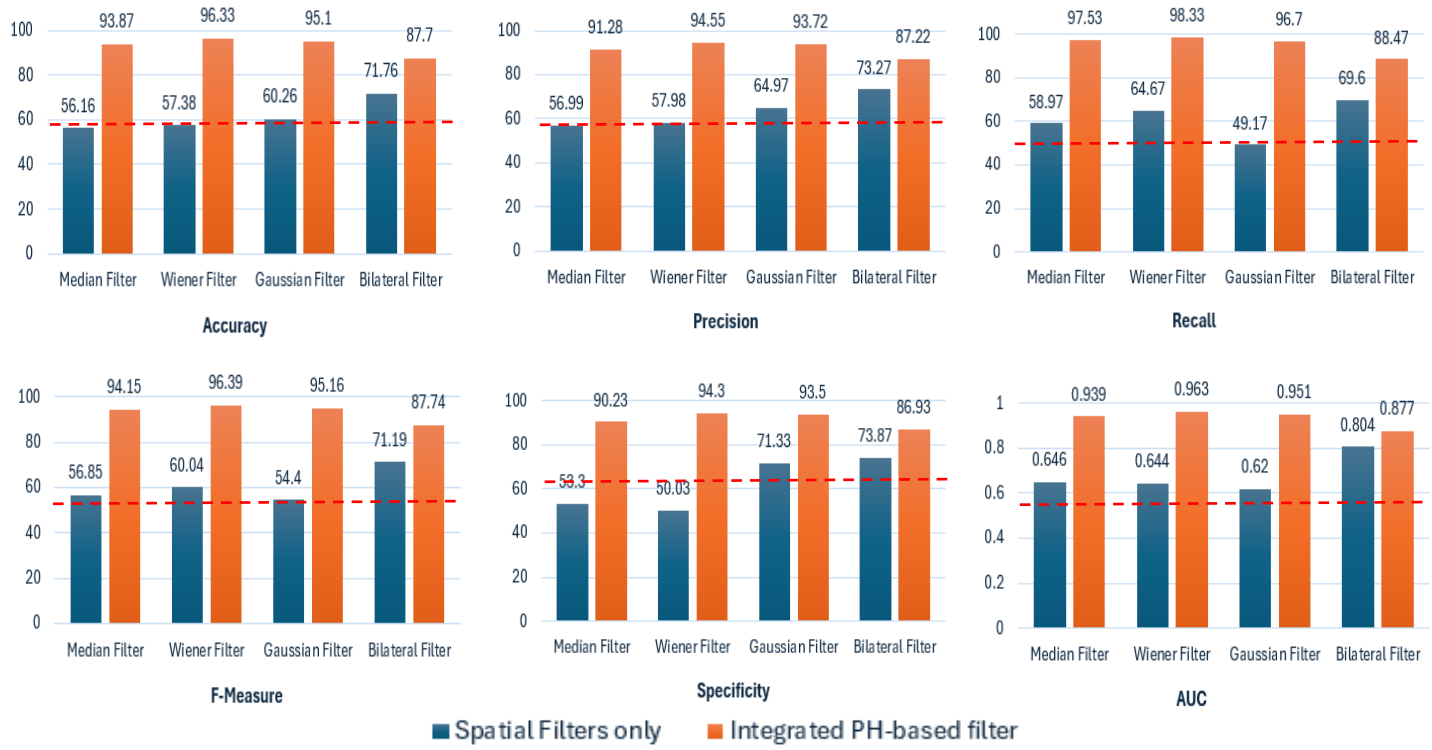

Figure 12. Comparison of classification performance metrics for spatial filters only and Integrated PH-based filter in the DDSM dataset

In Figure 12 (DDSM dataset), the Bilateral filter outperforms the original image across all metrics, both as a standalone filter and when integrated with PH-based filtering. When combined with PH-based filtering, all filters show significant improvements over the baseline, with the Wiener and Gaussian filters showing the most pronounced gains, especially in precision and recall. The Median filter also shows considerable improvement, especially in recall, indicating that PH integration helps these filters preserve critical topological features while improving classification performance. Notably, filters that initially performed poorly like the Median, Wiener, and Gaussian filters, show significant improvements after integration. Although the Bilateral filter already had the best standalone performance, also benefits from integration, though less pronounced compared to others, suggesting that PH provides more substantial benefits to filters that initially perform poorly.

In Figure 13 (MIAS dataset), both the Median and Bilateral filters outperform the original image in most metrics, with the Median filter demonstrating notable improvements in recall and precision. When integrated with PH-based filtering, the performance of all filters significantly improves compared to the

original image. Specifically, the Gaussian filter shows remarkable improvements in precision, recall, and F-measure, suggesting that PH-based filtering effectively enhances its ability to detect microcalcifications. The AUC for all filters also improves significantly when integrated with PH-based filtering, indicating better overall classification performance.

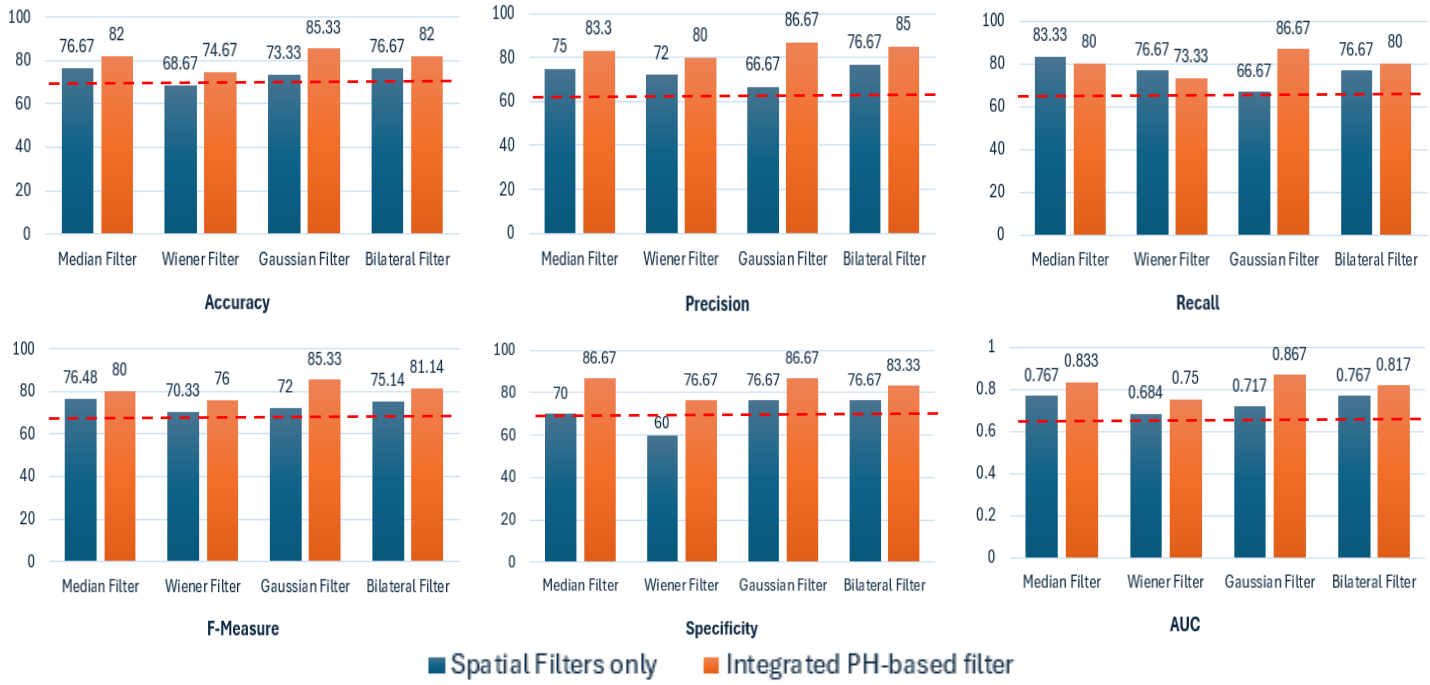

Figure 13. Comparison of classification performance metrics for spatial filters only and Integrated PH-based filter in the MIAS dataset

Comparing both datasets, we observe consistent patterns of improvement when integrating PH with spatial filters. However, the performance of individual filters varies between the DDSM and MIAS datasets. The degree of improvement is generally higher in the DDSM dataset. This can be attributed to the larger sample size in the DDSM dataset (244 images) compared to the MIAS dataset (26 images), which allows for a more robust evaluation of the filters' effectiveness.

In the DDSM dataset, the Wiener filter shows the greatest improvement when combined with PH-based filtering, achieving the highest accuracy, precision, recall, and AUC. This superior performance can be attributed to the Wiener filter's ability to handle varying noise levels, making it particularly effective for a diverse dataset like DDSM. The larger sample size allows the Wiener filter to adapt better to the differing noise characteristics present across the dataset, further enhancing its performance when combined with PH-based filtering. In contrast, in the MIAS dataset, the Gaussian filter outperforms others. The smaller sample size makes the results more sensitive to individual image variations. The Gaussian filter's smoothing capabilities balance noise reduction and preserve critical features such as microcalcifications. When integrated with PH-based filtering, the Gaussian filter effectively reduces noise while maintaining feature clarity, which explains its superior performance in the MIAS dataset. These variations highlight the importance of selecting filters that align with the specific dataset and image characteristics.

The results of this study align with the current literature, which emphasises the limitations of spatial filters alone and the need for advanced filtering techniques in medical image analysis. Traditional spatial filters often struggle with mammogram images' intrinsic heterogeneity and complex tissue structure, resulting in limited noise reduction and feature enhancement [42]. Integrating PH-based filtering addresses these limitations by enhancing the robustness of feature extraction, leading to more accurate and reliable classification outcomes.

Conclusions

This study demonstrates the effectiveness of the PH approach in evaluating and enhancing the classification performance of a neural network when spatial filters are applied to mammographic microcalcification images. By using PH, we transformed filtered images into PDs that capture topological features across multiple scales. These PDs were then vectorised using PH features and classified with a Neural Network Classifier. This evaluation revealed that traditional spatial filters, while reducing general noise, often fall short of fully eliminating noise and enhancing critical features necessary for accurate classification, resulting in suboptimal outcomes.

Integrating PH-based filter with spatial filters significantly enhances classification performance in mammographic microcalcifications images, as evidenced by improvements in accuracy, precision, recall, F-measure, specificity, and AUC across both DDSM and MIAS datasets. In the DDSM dataset, the Wiener filter's accuracy increased from 57.38% to 96.33%, while in the MIAS dataset, the Gaussian filter's accuracy improved from 73.33% to 85.33%. These findings highlight the potential of PH-based filtering to refine topological features and effectively reduce noise, thus enhancing diagnostic accuracy.

The study underscores the importance of evaluating spatial filters not just based on image quality metrics but also on their classification performance. The enhanced performance metrics validate the efficacy of this combined approach in early detection and diagnosis of breast cancer. For future research, several areas can be explored to advance the findings of this study. First, a comparative analysis between PH-based filtering with and without spatial filters could provide deeper insights into the specific contributions of each approach. Additionally, expanding the application of this method to larger and more diverse datasets will help validate its robustness and generalizability. Integrating this approach with other advanced image processing and machine learning models, such as deep learning architectures, could further enhance diagnostic accuracy. This line of research has the potential to contribute significantly to clinical outcomes by improving the early detection of breast cancer.

Conflicts of Interest

The author(s) declare(s) that there is no conflict of interest regarding the publication of this paper.

Acknowledgement

We gratefully acknowledge Universiti Kebangsaan Malaysia for the internal grant Tabung Agihan Pendapatan (TAP-K020061) . The first author would like to express her gratitude to Malaysia's Ministry of Higher Education (MOHE) and Universiti Teknologi MARA (UiTM) for the full SLAB scholarship. The authors thank the anonymous referees for their suggestions, which helped to improve this paper.

References

[1] Ferlay, J., *et al.* (2021). Cancer statistics for the year 2020: An overview. *International Journal of Cancer*, 148(4), 1–10. https://doi.org/10.1002/ijc.33588

[2] Arnold, M., *et al.* (2022). Current and future burden of breast cancer: Global statistics for 2020 and 2040. *The Breast*, 66, 15–23. https://doi.org/10.1016/j.breast.2022.08.010

[3] Ramadan, S. Z. (2020). Methods used in computer-aided diagnosis for breast cancer detection using mammograms: A review. *Journal of Healthcare Engineering*, 2020, 1–12. https://doi.org/10.1155/2020/9162464

[4] Htay, M. N. N., *et al.* (2021). Breast cancer screening in Malaysia: A policy review. *Asian Pacific Journal of Cancer Prevention*, 22(6), 1685. https://doi.org/10.31557/APJCP.2021.22.6.1685

[5] Yurdusev, A. A., Adem, K., & Hekim, M. (2023). Detection and classification of microcalcifications in mammogram images using difference filter and Yolov4 deep learning model. *Biomedical Signal Processing and Control*, 80, 1–7. https://doi.org/10.1016/j.bspc.2022.104360

[6] Azam, S., *et al.* (2021). Mammographic microcalcifications and risk of breast cancer. *British Journal of Cancer*, 125(5), 759–765. https://doi.org/10.1038/s41416-021-01459-x

[7] Loizidou, K., Skouroumouni, G., Nikolaou, C., & Pitris, C. (2020). An automated breast micro-calcification detection and classification technique using temporal subtraction of mammograms. *IEEE Access*, 8, 52785–52795. https://doi.org/10.1109/ACCESS.2020.2980616

[8] Almalki, Y. E., Soomro, T. A., Irfan, M., Alduraibi, S. K., & Ali, A. (2022). Impact of image enhancement module for analysis of mammogram images for diagnostics of breast cancer. *Sensors*, 22(1868), 1–20.

[9] Gowri, V., Valluvan, K. R., & Vijaya Chamundeeswari, V. (2018). Automated detection and classification of microcalcification clusters with enhanced preprocessing and fractal analysis. *Asian Pacific Journal of Cancer*

Prevention, 19(11), 3093–3098. https://doi.org/10.31557/APJCP.2018.19.11.3093

[10] Azam, A. S. B., Malek, A. A., Ramlee, A. S., Suhaimi, N. D. S. M., & Mohamed, N. (2020). Segmentation of breast microcalcification using hybrid method of Canny algorithm with Otsu thresholding and 2D wavelet transform. In *2020 10th IEEE International Conference on Control System, Computing and Engineering (ICCSCE)* (pp. 91–96). Penang, Malaysia. https://doi.org/10.1109/ICCSCE50387.2020.9204950

[11] Fadil, R., Jackson, A., El Majd, B. A., El Ghazi, H., & Kaabouch, N. (2020). Classification of microcalcifications in mammograms using 2D discrete wavelet transform and random forest. In *IEEE International Conference on Electro Information Technology* (pp. 353–359). https://doi.org/10.1109/EIT48999.2020.9208290

[12] Padmapriya, R., & Jeyasekar, A. (2022). Blind image quality assessment with image denoising: A survey. *Journal of Pharmaceutical Negative Results*, 13(3), 386–392. https://doi.org/10.47750/pnr.2022.13.S03.064

[13] Melekoodappattu, J. G., Subbian, P. S., & Queen, M. P. F. (2021). Detection and classification of breast cancer from digital mammograms using hybrid extreme learning machine classifier. *International Journal of Imaging Systems and Technology*, 31(2), 909–920. https://doi.org/10.1002/ima.22484

[14] Brito, F. A., Oliveira, H. C. R., Bakic, P. R., Maidment, A. D. A., & Vieira, M. A. C. (2016). Using bilateral filter to denoise digital mammograms acquired with reduced radiation dose. In *Congresso Brasileiro de Engenharia Biomédica* (pp. 1334–1337).

[15] Patil, R. S., & Biradar, N. (2020). Automated mammogram breast cancer detection using the optimized combination of convolutional and recurrent neural network. *Evolutionary Intelligence*, 14(4), 1459–1474. https://doi.org/10.1007/s12065-020-00403-x

[16] Rajaguru, H., & Sannasi Chakravarthy, S. R. (2020). Efficient denoising framework for mammogram images with a new impulse detector and non-local means. *Asian Pacific Journal of Cancer Prevention*, 21(1), 179–183. https://doi.org/10.31557/APJCP.2020.21.1.179

[17] Fan, L., Zhang, F., Fan, H., & Zhang, C. (2019). Brief review of image denoising techniques. *Visual Computing in Industry, Biomedicine, and Art*, 2(1), 7. https://doi.org/10.1186/s42492-019-0016-7

[18] Goyal, B., Dogra, A., Agrawal, S., Sohi, B. S., & Sharma, A. (2020). Image denoising review: From classical to state-of-the-art approaches. *Information Fusion*, 55, 220–244. https://doi.org/10.1016/j.inffus.2019.09.003

[19] Boby, S. M. (2021). Medical image denoising techniques against hazardous noises: An IQA metrics based comparative analysis. *I.J Image, Graphics and Signal Processing*, 2(April), 25–43. https://doi.org/10.5815/ijigsp.2021.02.03

[20] Spagnolo, F., Corsonello, P., Frustaci, F., & Perri, S. (2023). Design of approximate bilateral filters for image denoising on FPGAs. *IEEE Access*, 11, 1990–2000. https://doi.org/10.1109/ACCESS.2022.3233921

[21] Boby, S. M. (2021). Medical image denoising techniques against hazardous noises: An IQA metrics based comparative analysis. *I.J Image, Graphics and Signal Processing*, 2(April), 25–43. https://doi.org/10.5815/ijigsp.2021.02.03

[22] Kshema, M. J. George, & Dhas, D. A. S. (2017). Preprocessing filters for mammogram images: A review. In *2017 Conference on Emerging Devices and Smart Systems (ICEDSS)* (pp. 1–7). https://doi.org/10.1109/ICEDSS.2017.8073694

[23] Kusano, G., Fukumizu, K., & Hiraoka, Y. (2018). Kernel method for persistence diagrams via kernel embedding and weight factor. *Journal of Machine Learning Research*, 18, 1–41.

[24] Sapini, M. L., Noorani, M. S. M., Razak, F. A., Alias, M. A., & Yusof, N. M. (2022). Understanding published literatures on persistent homology using social network analysis. *Malaysian Journal of Fundamental and Applied Sciences*, 18(4), 413–429. https://doi.org/10.11113/mjfas.v18n4.2418

[25] Qaiser, T., Tsang, Y. W., Epstein, D., & Rajpoot, N. (2017). Tumor segmentation in whole slide images using persistent homology and deep convolutional features. *Communications in Computer and Information Science*, 723, 320–329. https://doi.org/10.1007/978-3-319-60964-5_28

[26] Assaf, R., Goupil, A., Kacim, M., & Vrabie, V. (2017). Topological persistence based on pixels for object segmentation in biomedical images. In *International Conference on Advances in Biomedical Engineering (ICABME)* (pp. 1–6). https://doi.org/10.1109/ICABME.2017.8167531

[27] Teramoto, T., Shinohara, T., & Takiyama, A. (2020). Computer-aided classification of hepatocellular ballooning in liver biopsies from patients with NASH using persistent homology. *Computers in Biology and Medicine*, 195, 105614. https://doi.org/10.1016/j.cmpb.2020.105614

[28] Rammal, A., Assaf, R., Goupil, A., Kacim, M., & Vrabie, V. (2022). Machine learning techniques on homological persistence features for prostate cancer diagnosis. *BMC Bioinformatics*, 23(1), 1–22. https://doi.org/10.1186/s12859-022-04992-5

[29] Asaad, A., Ali, D., Majeed, T., & Rashid, R. (2022). Persistent homology for breast tumor classification using mammogram scans. *Mathematics*, 10(21), 1–13. https://doi.org/10.3390/math10214039

[30] Oyama, A., *et al.* (2019). Hepatic tumor classification using texture and topology analysis of non-contrast-enhanced three-dimensional T1-weighted MR images with a radiomics approach. *Scientific Reports*, 9(1), 2–11. https://doi.org/10.1038/s41598-019-45283-z

[31] Avilés-Rodríguez, G. J., *et al.* (2021). Topological data analysis for eye fundus image quality assessment. *Diagnostics, 11*(8). https://doi.org/10.3390/diagnostics11081322

[32] Malek, A. A., Alias, M. A., Razak, F. A., Noorani, M. S., Mahmud, R., & Zulkepli, N. F. (2023). Persistent homology-based machine learning method for filtering and classifying mammographic microcalcification images in early cancer detection. *Cancers, 15*(9). https://doi.org/10.3390/cancers15092606

[33] Hu, C. S., Lawson, A., Chen, J. S., Chung, Y. M., Smyth, C., & Yang, S. M. (2021). Toporesnet: A hybrid deep learning architecture and its application to skin lesion classification. *Mathematics, 9*(22), 1–22. https://doi.org/10.3390/math9222924

[34] Atienza, N., Escudero, L. M., & Jimenez, M. J. (2019). Persistent entropy: A scale-invariant topological statistic for analysing cell arrangements, 1–14.

[35] Leykam, D., Rondón, I., & Angelakis, D. G. (2022). Dark soliton detection using persistent homology. *Chaos: An Interdisciplinary Journal of Nonlinear Science, 32*(7), 73133. https://doi.org/10.1063/5.0097053

[36] Rammal, A., Assaf, R., Goupil, A., Kacim, M., & Vrabie, V. (2022). Machine learning techniques on homological persistence features for prostate cancer diagnosis. *BMC Bioinformatics, 23*(1), 1–22. https://doi.org/10.1186/s12859-022-04992-5

[37] Adams, H., *et al.* (2017). Persistence images: A stable vector representation of persistent homology. *Journal of Machine Learning Research, 18*, 1–35.

[38] Teramoto, T., Shinohara, T., & Takiyama, A. (2020). Computer-aided classification of hepatocellular ballooning in liver biopsies from patients with NASH using persistent homology. *Comput Methods Programs Biomed, 195*. https://doi.org/10.1016/j.cmpb.2020.105614

[39] Asaad, A., Ali, D., Majeed, T., & Rashid, R. (2022). Persistent homology for breast tumor classification using mammogram scans. *Mathematics, 10*(21). https://doi.org/10.3390/math10214039

[40] Suckling, J. (1994). The mammographic image analysis society digital mammogram database. *Exerpta Medica International Congress*, 375–386.

[41] Heath, M., Bowyer, K., Kopans, D., Moore, R., & Kegelmeyer, P. (2000). The digital database for screening mammography. In *Fifth International Workshop on Digital Mammography* (pp. 212–218). Toronto, Canada.

[42] Goyal, B., Dogra, A., Agrawal, S., Sohi, B. S., & Sharma, A. (2020). Image denoising review: From classical to state-of-the-art approaches. *Information Fusion, 55*(September 2019), 220–244. https://doi.org/10.1016/j.inffus.2019.09.003

[43] Michael, E., Ma, H., Li, H., Kulwa, F., & Li, J. (2021). Breast cancer segmentation methods: Current status and future potentials. *Biomed Res Int, 2021*. https://doi.org/10.1155/2021/9962109

[44] Garg, S., Vijay, R., & Urooj, S. (2019). Statistical approach to compare image denoising techniques in medical MR images. *Procedia Comput Sci, 152*, 367–374. https://doi.org/10.1016/j.procs.2019.05.004

[45] Zhang, X., Gao, W., Zhu, S., & Engineering, I. (2020). Research on noise reduction and enhancement of weld image. In *9th International Conference on Signal, Image Processing and Pattern Recognition (SPPR 2020)* (pp. 13–26). https://doi.org/10.5121/csit.2020.101902

[46] Ramadan, Z. M. (2018). Optimum image filters for various types of noise. *TELKOMNIKA, 16*(5), 2458–2464. https://doi.org/10.12928/TELKOMNIKA.v16i5.10508

[47] Rybakova, E. O., Limonova, E. E., & Nikolaev, D. P. (2024). Fast Gaussian filter approximations comparison on SIMD computing platforms. *Applied Sciences, 14*(11). https://doi.org/10.3390/app14114664

[48] Ramadan, S. Z. (2020). Methods used in computer-aided diagnosis for breast cancer detection using mammograms: A review. *J Healthc Eng, 2020*. https://doi.org/10.1155/2020/9162464

[49] Günther, D., Jacobson, A., Reininghaus, J., Seidel, H. P., Sorkine-Hornung, O., & Weinkauf, T. (2014). Fast and memory-efficient topological denoising of 2D and 3D scalar fields. *IEEE Trans Vis Comput Graph, 20*(12), 2585–2594. https://doi.org/10.1109/TVCG.2014.2346432

[50] Fan, L., Zhang, F., Fan, H., & Zhang, C. (2019). Brief review of image denoising techniques. *Vis Comput Ind Biomed Art, 2*(1), 7. https://doi.org/10.1186/s42492-019-0016-7

[51] Avilés-Rodríguez, G. J., *et al.* (2021). Topological data analysis for eye fundus image quality assessment. *Diagnostics, 11*(8). https://doi.org/10.3390/diagnostics11081322

[52] Otter, N., Porter, M. A., Tillmann, U., Grindrod, P., & Harrington, H. A. (2017). A roadmap for the computation of persistent homology. *EPJ Data Sci, 6*, 1–38.

[53] Garin, A., & Tauzin, G. (2019). A topological 'reading' lesson: Classification of MNIST using TDA. In *Proceedings - 18th IEEE International Conference on Machine Learning and Applications, ICMLA 2019* (pp. 1551–1556). https://doi.org/10.1109/ICMLA.2019.00256

[54] Adams, H., *et al.* (2017). Persistence images: A stable vector representation of persistent homology. *Journal of Machine Learning Research, 18*, 1–35.

[55] Iqbal, S., Qureshi, A. N., Li, J., & Mahmood, T. (2023). On the analyses of medical images using traditional machine learning techniques and convolutional neural networks. *Springer Netherlands, 30*(5). https://doi.org/10.1007/s11831-023-09899-9

[56] Jiao, Y., & Du, P. (2016). Performance measures in evaluating machine learning based bioinformatics predictors for classifications. *Quantitative Biology, 4*(4), 320–330. https://doi.org/10.1007/s40484-016-0081-2

[57] Yurdusev, A. A., Adem, K., & Hekim, M. (2023). Detection and classification of microcalcifications in mammograms images using difference filter and Yolov4 deep learning model. *Biomed Signal Process Control, 80*. https://doi.org/10.1016/j.bspc.2022.104360

[58] Kaji, S., Sudo, T., & Ahara, K. (2020). Cubical Ripser: Software for computing persistent homology of image and volume data. *D, 1–9*. Retrieved from http://arxiv.org/abs/2005.12692